Correlations in Charged Multipore Systems: Implications for Enhancing Selectivity and Permeability in Nanoporous Membranes

Brian A. Shoemaker, Omar Khalifa, and Amir Haji-Akbari*

Cite This: https://doi.org/10.1021/acsnano.3c07489

Read Online

ACCESS | Metrics & More | Article Recommendations | SI Supporting Information

ABSTRACT: Nanoporous membranes have emerged as powerful tools for diverse applications, including gas separation and water desalination. Achieving high permeability for desired molecules alongside exceptional rejection of other species presents a significant design challenge. One potential strategy involves optimizing the chemistry and geometry of isolated nanopores to enhance permeability and selectivity while maximizing their density within a membrane. However, the impact of the pore proximity on membrane performance remains an open question. Through path sampling simulations of model graphitic membranes with multiple subnanometer pores, we reveal that nanoscale proximity between pores detrimentally affects water permeability and salt rejection. Specifically, counterion transport is decelerated, while co-ion transport is accelerated, due to direct interactions among water molecules, salt ions, and the dipoles within neighboring pores. Notably, the observed ionic transport time scales significantly deviate from established theories such as the access resistance model but are well explained using the simple phenomenological model that we develop in this work. We use this model to prescreen and optimize pore arrangements that elicit minimal correlations at a target pore density. These findings deepen our understanding of multipore systems, informing the rational design of nanoporous membranes for enhanced separation processes such as water desalination. They also shed light on the physiology of biological cells that employ ion channel proteins to modulate ion transport and reversal potentials.

KEYWORDS: nanofluidics, nanopores, molecular simulations, advanced sampling, desalination; selectivity
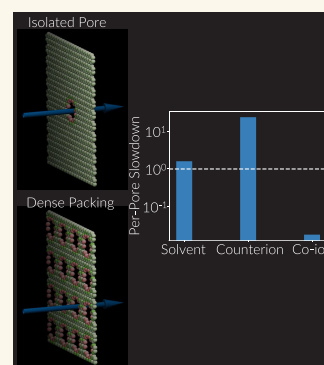
INTRODUCTION

Nanoporous materials offer excellent prospects for advancing membrane technology, particularly for separation applications. Within the confines of nanopores, molecules can directly interact with pore walls, giving rise to intriguing phenomena that defy conventional transport theories.[1] Moreover, the ability to finely tune the geometry and chemistry of such nanopores enables us to engineer separation modalities based on size, shape, electrostatic charge, and directional interactions such as hydrogen bonding.[2] This exciting frontier makes it possible to design innovative membrane systems with increased precision and efficiency. In recent decades, a wide variety of nanoporous membranes based on materials such as graphene,[3−6] polymers,[7−9] silicon,[10,11] alumina,[12,13] and metal organic frameworks[14−20] have been demonstrated to exhibit promising performance in a range of applications such as desalination,[3,4,6,8,9] virus filtration,[7] power generation,[10,21] biomolecule separation,[12] molecule detection,[13] gas storage,[14,18−20] catalysis,[15] and drug delivery.[16,17]

In designing membranes for separation applications, it is essential to maximize the permeability of desired species while maintaining a satisfactory level of selectivity against undesirable species. As an example, take reverse osmosis (RO) desalination, a critical technology for sustainable and accessible freshwater supply.[22−25] An effective RO membrane must have high water permeability and strong selectivity against small ionic and molecular solutes. Achieving high selectivity is necessary to ensure sufficiently low impurity concentrations in the product, while high water permeability plays a vital role in reducing energy consumption and operational costs. Unfortunately, selectivity and permeability often exhibit an inverse correlation, making it challenging to enhance one without compromising the other.[26] To overcome this paradigm, a promising approach entails optimizing the chemistry and geometry of isolated nanopores to achieve the desired permeability and selectivity while leveraging advanced syn-

thesis and fabrication techniques to incorporate as many of these optimized nanopores as feasible within nanoporous membranes. Assuming that such pores will act independently, permeability will scale with pore density, while selectivity will remain unaffected. However, significant knowledge gaps exist regarding the potential impact of proximal pores on each other's permeability and selectivity, and the applicability of existing theories such as the access resistance model[27,28] to regimes relevant to ultraselective membrane separation has yet to be rigorously tested. Addressing this question is not only crucial from a practical perspective but also essential for the predictive multiscale modeling of transport through porous materials.

In this study, we employ nonequilibrium molecular dynamics (NEMD) simulations[29] and jumpy forward flux sampling (JFFS)[30] to probe the kinetics of water and ion transport through model multipore graphitic membranes with subnanometer pores whose interiors are decorated with permanent dipoles. We observe that the transport of counterions experiences a drastic slowdown due to direct interactions between the leading ion and the dipoles in neighboring pores, surpassing the predictions of established theories by up to an order of magnitude. Conversely, these very dipole–ion interactions trigger an enhancement in co-ion transport. Moreover, the water permeability experiences a slight reduction, primarily attributed to dipole–dipole interactions. Notably, these findings have direct implications for water desalination processes, as the introduction of a larger number of charged pores within a porous material can result in diminished solvent–solute selectivity.

RESULTS AND DISCUSSION

We first use JFFS to compute the transport time scales for chloride ions, which, according to our earlier works,[5,6] are the first to traverse the hydrogen-passivated pores considered here. We consider pore arrangements depicted in Figure 1C–G. In the case of independent pore behavior, τ_n, the mean translocation time scale for an n-pore system can be expressed as $\tau_n = \tau_1/n$. Consequently, we employ $n\tau_n/\tau_1$ as a measure of the correlation among n pores. Values greater than unity indicate a slowdown due to pore proximity, while values less than one imply acceleration. We find chloride transport to be significantly impeded by pore proximity, as is evident from Table 1 and Figure 2B. Furthermore, the slowdown in chloride transport becomes more pronounced with an increased number of pores in the system, with the magnitude of deceleration dependent on both the number and arrangement of the pores. For instance, a linear arrangement of three pores results in a smaller slowdown compared to a triangular arrangement. The most substantial deceleration is observed in the membrane fully covered with 64 identical nanopores, where chloride transport experiences a striking 23-fold reduction in flux.

To elucidate the origin of the observed slowdown, we compare our computed slowdowns with predictions from the access resistance model, initially proposed by Hille[27] and further developed by Hall[28] for estimating ionic conductance through nanoporous membranes under an external electric field.[31] Figure 2A illustrates the major resistances to ionic current under such a scenario: two access resistances ($R_{a,n}$) between the electrodes and pore openings, and the pore resistance ($R_{p,n}$) with the circuit resistance given by $2R_{a,n} + R_{p,n}$. According to this model, applicable to weakly charged pores
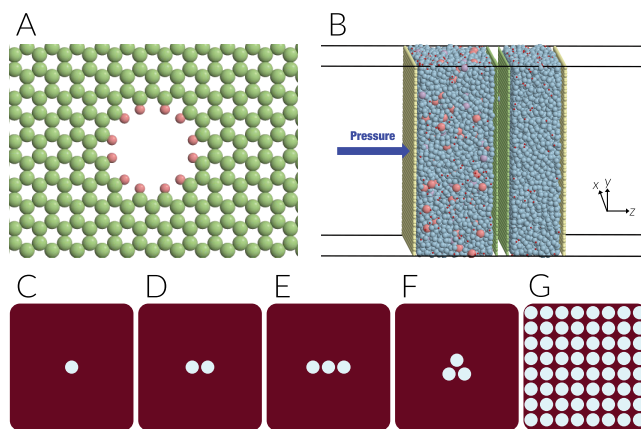
Figure 1. (A) A single subnanometer circular pore within a graphene sheet and passivated by hydrogen atoms. (B) Simulation box with a three-layer graphitic membrane with each layer containing one or several pores of the type shown in (A). Sodium (light purple) and chloride (dark orange) ions and water molecules (light blue) are present in the feed compartment, while the filtrate only contains water. Pressure gradient is applied using the graphene pistons (yellow). Carbon and hydrogen atoms in the membrane are shown in green and light red, respectively. (C–G) Schematic representation of (C) one-pore, (D) two-pore, (E) three-pore linear, (F) three-pore triangular, and (G) full coverage pore arrangements.

with diffusion-limited ion transport, pore proximity increases only $R_{a,n}$, while $R_{p,n}$ is determined by $R_{p,n}^{-1} = \sum_{k=1}^{n} R_k^{-1}$, where R_k represents the resistance of isolated pore k. For n identical pores, the overall slowdown will be given by[32]

$$S = 1 + \frac{\pi}{2n\beta(\pi + 4\alpha)} \sum_{i,j=1,i \neq j}^{n} \frac{1}{|\mathbf{s}_j - \mathbf{s}_i|} \tag{1}$$

Here, $\alpha = h/d$ and $\beta = l/d$ denote two aspect ratios, with d and h as the pore diameter and length, respectively, and l as a characteristic length scale for pore spacing. $\mathbf{s}_i = \mathbf{r}_i/l$ represents the reduced position of pore i on the membrane surface. Although ions encounter resistance during pore approach, entry, and exit in our study, they traverse the nanoporous membrane under pressure and chemical potential gradients rather than an electric field and their transport is not diffusion-limited. All of these factors limit the expected relevance of the access resistance model. Nonetheless, we still use it as an existing benchmark to assess the extent to which the observed slowdown can be attributed solely to changes in the access resistance.

Figure 2B displays the slowdowns in chloride transport for all multipore systems, along with the predicted values from the access resistance model. It is important to highlight that no closed-form extension of Equation 1 exists for periodic domains, despite attempts to investigate the scaling of access resistance with periodic box dimensions.[33] Therefore, our estimates of S may contain small, unquantifiable systematic errors, particularly for the full coverage system. However, even accounting for possible periodicity corrections, the slowdowns computed from path sampling simulations will significantly exceed that of the access resistance model. This discrepancy also grows with the number of pores. In the full coverage system in particular, the access resistance model predicts a slowdown of 2.51, whereas direct rate calculations reveal an actual slowdown of 23.4. Therefore, the access resistance

Table 1. Chloride Transport Time Scales Computed from JFFS Simulations Compared with Predictions of the Access Resistance Model[a]

System	$\tau_{Cl,n}$ (ns)	$n\tau_{Cl,n}$ (ns)	$S = n\tau_{Cl,n}/\tau_{Cl,1}$	$S_{access\ resistance}$
One-pore	49 ± 22.4	49 ± 22.4	1.00	1.00
Two-pore	51.4 ± 3.9	102.8 ± 7.8	2.10 ± 0.96	1.08 ± 1.12
Three-pore linear	44.6 ± 3.8	133.9 ± 11.4	2.73 ± 1.25	1.12 ± 0.09
Three-pore triangular	72.7 ± 10.2	218.1 ± 30.6	4.45 ± 2.09	1.15 ± 0.10
Full coverage	17.9 ± 2.4	1146.1 ± 153.5	23.40 ± 11.0	2.51 ± 1.08

[a]All uncertainties correspond to 95% confidence intervals.
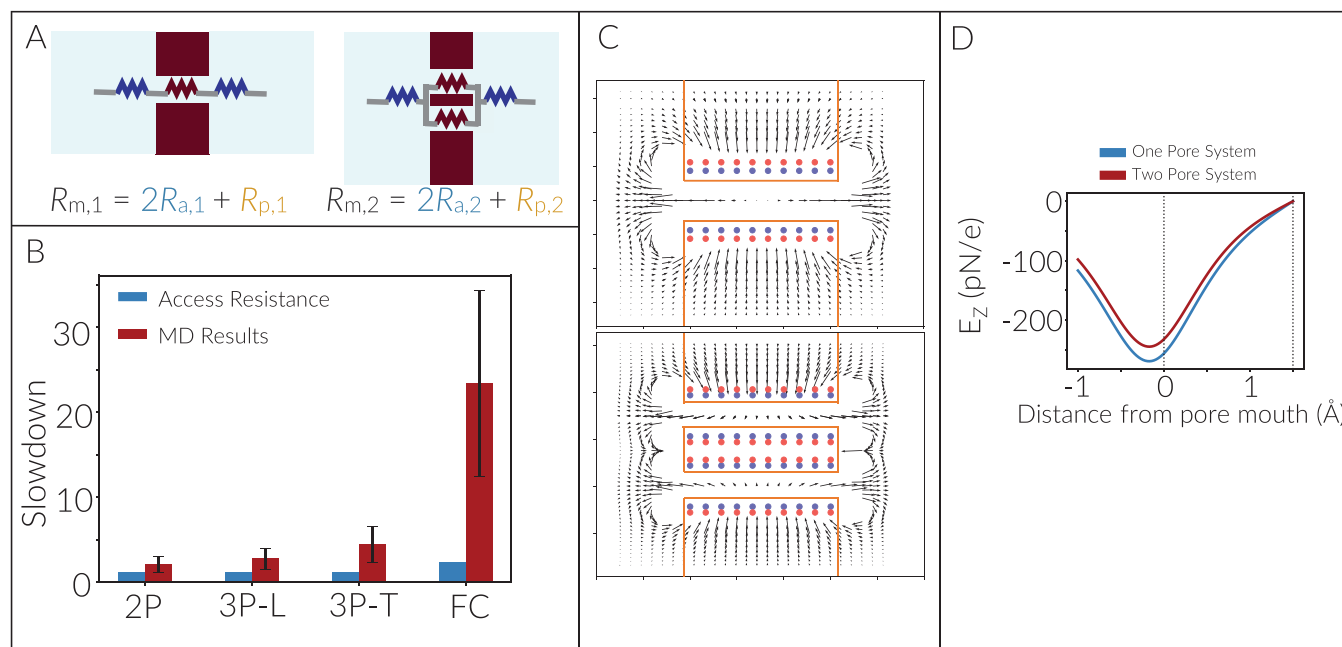
Figure 2. (A) Schematic illustration of key resistors to ion transport through a nanoporous membrane. According to the access resistance model, pore proximity affects only the access resistance ($R_{a,2} > R_{a,1}$) while pore resistance remains constant regardless of pore number and separation. (B) Comparison of observed chloride transport slowdowns with access resistance model predictions, with significant underestimation by the model. (C) Electric field profiles in model one- and two-pore systems, where neighboring pore dipoles interfere destructively along the central axis, weakening the electric field. (D) The electric field along the pore axis in both the single-pore and two-pore models demonstrating that the presence of a neighboring pore diminishes the magnitude of the electric field.

model functions as a negative control to demonstrate that the observed slowdowns cannot be solely explained by changes to access resistance. It is worthwhile to note that extensions[34−40] of the access resistance model have been developed to assess changes in pore resistance for nearby pores, but as they are based on solutions of the classical Poisson-Nernst−Planck (PHP) equation,[41,42] they are of limited utility for pores with subnanometer dimensions that elicit nondiffusive hindered transport.

These observed deviations from the access resistance model raise the possibility that pore proximity might also impact the resistances of individual pores. This is also bolstered by the observation that in membranes wherein different pores are not equivalent the leading chloride does not visit all pores with equal probability. For instance, in the membrane with three linearly arranged pores, a chloride is more likely to traverse the peripheral pores, implying that those exert less resistance to translocation than the central pore. Indeed, the pores considered in this work are not weakly charged (as assumed in access resistance theory) but are decorated by fixed dipoles. As as can be seen in Figure 2C, these dipoles point toward the central axis of the pore and generate an electric field that points

away from the pore center in both directions. This electric field is indeed responsible for pulling in the chlorides as counterions and preferring them over sodiums. The introduction of a second pore in the proximity of the initial pore results in the attenuation of the electric field generated by the dipole moments of the original pore. This reduction occurs due to the opposing orientation of the neighboring pore's dipoles, which collectively exert repulsive forces on the predominant chloride ions.

To quantify the impact of dipoles within neighboring pores on the observed slowdowns, we calculated the potential energetic penalty experienced by a bare chloride as it translocates through an empty pore. The calculated penalties, depicted in Figure 3A, are positive in all cases, indicating an increase in the free energy barrier and a slowdown in translocation kinetics. Increasing the number of neighboring pores amplifies this penalty due to the greater destabilizing effect of the additional neighboring dipoles on the leading chloride. Additionally, in membranes with three pores, the penalty varies among individual pores, consistent with the traversal probabilities obtained from JFFS calculations. For instance, in a linear arrangement of three pores, the central
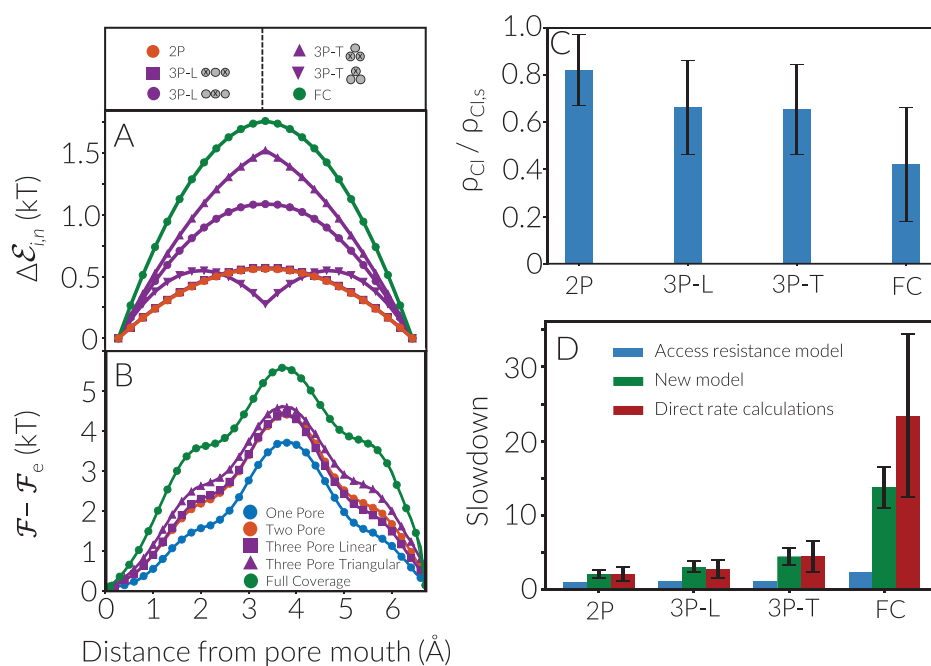
Figure 3. (A) Potential energetic penalty experienced by leading anions due to interacting with neighboring pore dipoles. (B) Change in free energy of the leading chloride upon entering the pore computed from the FFS-MFPT method.[43] $\mathcal{F}_e$ corresponds to free energy at the pore entrance. (C) Chloride concentration near pore openings in multipore systems compared to its single-pore counterpart. (D) Slowdowns computed from FFS (red) and predicted from the access resistance model (blue) and eq 3 based on ion−dipole interactions (green).

pore incurs a higher penalty due to its exposure to neighboring dipoles on both sides compared with the peripheral pores. Accordingly, we observe that the leading chloride ion translocates through the central pore only 22% of the time while passing through each peripheral pore 39% of the time. Note that the energetic penalties in the peripheral pores closely resemble those in the two-pore system, given the short-range of dipole−ion interactions. Even in the case of triangularly arranged pores with symmetrical pore openings, a significant disparity in energetic penalties (and corresponding translocation probabilities) exists between the top and bottom pores, attributable to the parallel shift between the graphene sheets in the graphite structure. Interestingly, the computed energetic penalties are consistent with changes in the translocation free energy inside the pore as computed by JFFS (shown in Figure 3B and Table 2) suggesting that these ion-dipole interactions are the primary factor impacting the free energetics of ion transport within the pore.

Table 2. Potential Energetic Penalty Experienced by the Leading Chloride Inside the Pore of an *n*-Pore System vs the Change in the Free Energy Barrier Computed from JFFS[a]

System	$\beta[\Delta\mathcal{F}_n^* - \Delta\mathcal{F}_s^*]$	$\beta\Delta\mathcal{E}_n$
2P	0.70	0.56
3P-L	0.75	0.71
3P-T	0.91	1.07
FC	1.87	1.76

[a]Here, $\Delta\mathcal{F}_n^*$ and $\Delta\mathcal{F}_s^*$ correspond to translocation barriers in the *n*- and one-pore systems, respectively, and $\beta\Delta\mathcal{E}_n = -\ln[\sum_{i=1}^n e^{-\beta\Delta\mathcal{E}_{i,n}}/n]$. For proper comparison among different systems, the pore entrance is used as a point of reference in estimating $\Delta\mathcal{F}^*$ in each system.

Despite qualitative predictability, the energetic penalties alone cannot quantitatively account for the observed slowdown. For instance, the predicted energetic penalty of approximately $1.8k_BT$ in the full coverage system would only correspond to a 6-fold slowdown, significantly smaller than the 23-fold slowdown from JFFS calculations. This discrepancy can be explained by noting the destabilization of chlorides within the feed by dipoles in neighboring pores, hindering their approach to pore opening. Predicting this effect accurately is challenging due to factors such as hydration, entropic effects, and ion-graphene interactions. However, its existence can be confirmed quantitatively by evaluating chloride concentration at the pore opening within the $F_{0,0}$ basin. We assess this by computing the chloride concentration within a hemispheric region (of radius 2.32 Å) centered at each pore opening. As illustrated in Figure 3C, the prepore chloride concentration significantly decreases in multipore systems, with a larger decline observed in systems with more pores. Consequently, the rate of partitioning into the membrane decreases, leading to a reduced flux term in the rate expression. (Due to differences in the optimal placements of FFS milestones in different systems, it is not feasible to confirm this via direct flux comparisons across different FFS calculations.)

By leveraging these observations, we can construct a simple model to predict ionic slowdown based on assumptions of single-step transport kinetics with an Arrhenius-type temperature dependence, $\mathcal{J} = \mathcal{A}e^{-\beta\Delta\mathcal{F}}$. Here, $\mathcal{J}$ represents chloride flux, while $\mathcal{A}$ and $\Delta\mathcal{F}$ correspond to the kinetic prefactor and the free energy barrier, respectively. We anticipate that the prepore chloride concentration ρ_{Cl} and the dipole-induced energetic penalty $\Delta\mathcal{E}$ primarily affect $\mathcal{A}$ and $\Delta\mathcal{F}$, respectively. As a first approximation, we assume $\mathcal{A} \propto \rho_{Cl}$ and $\Delta\mathcal{F}_{i,n} \approx \Delta\mathcal{F}_s + \Delta\mathcal{E}_{i,n}$, where indices s and *i,n* refer to a single pore and the *i*th pore within an *n*-pore configuration,

respectively. (The latter assumption is already confirmed based on the data presented in Table 2.) The slowdown for pore i will then be given by

$$\mathcal{S}_i = \frac{\mathcal{J}_s}{\mathcal{J}_{i,n}} \approx \frac{\rho_{\text{Cl,s}}}{\rho_{\text{Cl},i,n}} e^{\beta \Delta \mathcal{E}_{i,n}} \tag{2}$$

For systems with multiple distinct pores (e.g., three-pore systems), the overall slowdown S can be estimated from

$$\frac{1}{S} = \frac{1}{n} \sum_{i=1}^{n} \frac{1}{S_i} \tag{3}$$

This model can be readily extended to directly compare various multipore arrangements. This might be occasionally necessary considering the larger uncertainties in prepore chloride concentration in the single-pore system.

As shown in Figure 3D, the predictions obtained using eq 3 align well with the FFS-computed slowdowns, surpassing the predictions of the access resistance model. This confirms that the destabilizing effect of neighboring dipoles on the leading chloride primarily accounts for the observed slowdown and leads to a significant increase in the pore interior resistance.

We need to emphasize that there are uncertainties affecting the quantitative predictability of eqs 2 and 3, potentially contributing to the observed discrepancies with the slowdowns obtained from direct rate calculations. One factor is the definition of the prepore region, which lacks a first-principles basis, and although our choice is reasonable, alternative definitions could alter our quantitative predictions. Additionally, the influence of neighboring dipoles on trailing ions within the feed and the resulting changes in their distribution and the electrostatic forces that they exert are even more difficult to quantify and are therefore not accounted for here. To qualitatively understand the effect of chloride transport on charge distribution in the feed, we partition the membrane surface into three regions: (i) the area outside the traversed pore, (ii) the area outside adjacent pores, and (iii) the remainder of the membrane. Figure 4 illustrates the change in charge density relative to a one-pore system for each region. Notably, areas (i) and (iii) become more positively charged,
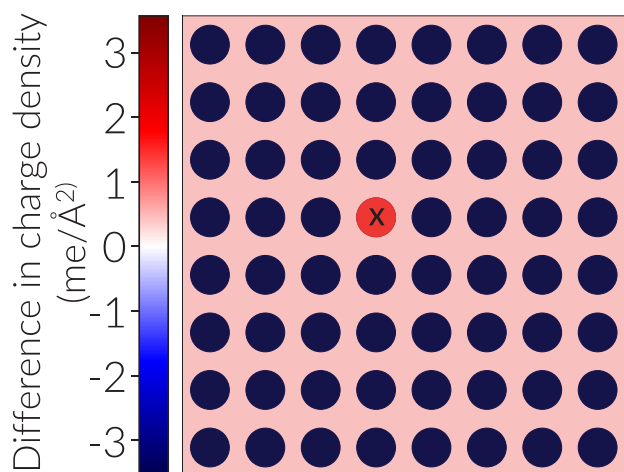
while (ii) becomes more negatively charged due to the affinity of unoccupied pores for chlorides. The magnitude of these changes governs the nature of ion—ion interactions, which is challenging to predict by using a simple theory. However, we anticipate that these changes will have the most significant impact in the full-coverage system, where we observe the largest, and yet statistically insignificant, discrepancy between our model and the actual slowdowns.

To investigate the impact of pore density on selectivity, it is necessary to examine the transport of subsequent ions, specifically sodium, after a chloride ion has traversed the membrane (i.e., the $F_{0,1} \to F_{1,1}$ transition). The charge separation resulting from chloride transport creates a strong driving force for sodium transport as the co-ion. Secondary sodium transport time scales are significantly larger than those of chloride. In the one-pore system, for instance, we estimate the $F_{0,1} \to F_{1,1}$ transition time scale to be 1077 ± 367 s, about 10 orders of magnitude larger than the $F_{0,0} \to F_{0,1}$ transition time scale. Due to prohibitively large computational costs, we only conducted the $F_{0,1} \to F_{1,1}$ calculation for the full coverage system to observe the largest possible impact and compute the transport time scale to be $\tau_n = 0.29 \pm 0.04$ s. This implies a nearly 58-fold reduction in per-pore transport time scale, highlighting the distinctive behavior of sodium transport in the full-coverage system, which qualitatively contrasts the access resistance model's prediction of slowdown for all ions.

The astounding enhancement of sodium transport can be attributed to the direct dipole—ion interactions, which simultaneously destabilize the counterion and stabilize the co-ion. The energetic penalty experienced by the leading counterion due to neighboring pore dipoles is equivalent in magnitude to the energetic gain achieved by the leading co-ion within the pore (Figure 5). Additionally, the reduction in

Figure 5. Potential energetic gain of sodium in a pore due to its interaction with neighboring pore dipoles in the full coverage system.
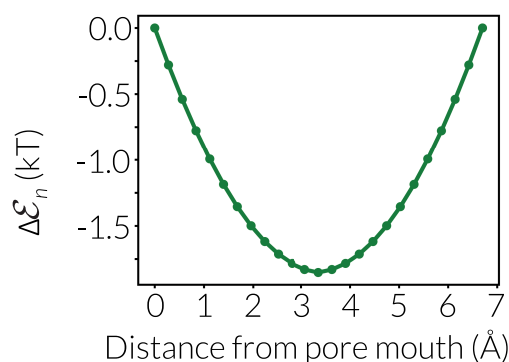
Figure 4. Changes in charge density on the membrane surface with respect to the single-pore system. Additional pores lead to a higher chloride concentration near their openings but lower chloride and higher sodium concentrations elsewhere.

electric field strength at the pore opening, which results in decreased chloride concentration in the prepore region, leads to a higher concentration of sodium in the same region. In the full-coverage system, sodium ions are prominently present near the pore openings, while they are nearly absent in the one-pore system. This increase in concentration, which is difficult to quantify due to the absence of sodiums at the pore opening in the one-pore system, will inevitably enhance the kinetics of sodium transport, in conjunction with the potential energetic gain depicted in Figure 5.

In order to comprehensively analyze the impact of pore density on solvent−solute selectivity, we investigate the effect of pore proximity on the rates of water transport. Despite their electric neutrality, water molecules possess dipole moments and can also interact with electric fields. Therefore, variations in the electric field strength caused by dipoles within neighboring pores can affect their transport as well. Table 3

Table 3. Water Transport Time Scales Obtained from Conventional NEMD Simulations[a]

| System	$\tau_{w,n}$ (ps)	$n\tau_{w,n}$ (ps)	$n\tau_{w,n}/\tau_{w,1}$
One-pore	435 ± 203	435 ± 203	1.00
Two-pore	235 ± 59	470 ± 118	1.08 ± 0.53
Three-pore linear	165 ± 35	495 ± 195	1.14 ± 0.51
Three-pore triangular	221 ± 65	663 ± 495	1.52 ± 0.55
Full coverage	11.0 ± 0.6	704 ± 38	1.61 ± 0.47

[a]All uncertainties correspond to 95% confidence intervals.

presents the average passage times of water molecules through membranes with different pore arrangements. While a slight slowdown in water transport is observed in all cases, a slowdown is only statistically significant in the full-coverage system.

The slowdown in water transport can be attributed to the alignment of water molecules' dipole moments with the electric field. Figure 6B−G demonstrates that oxygen atoms of water molecules in the first liquid layer adjacent to the membrane or within the pore tend to point toward the pore interior. Since the strength of the electric field varies with distance from the pore, for water molecules approaching the pore entrance in this preferred orientation, the magnitude of the force exerted on the oxygen atom exceeds the force exerted on hydrogens, causing the molecule to be pulled into the pore. Likewise, electrostatic interactions between water molecules and the dipoles at the pore interior will inhibit water from exiting the membrane. Since entry to the pore is already accompanied by an energetically unfavorable partial loss of the
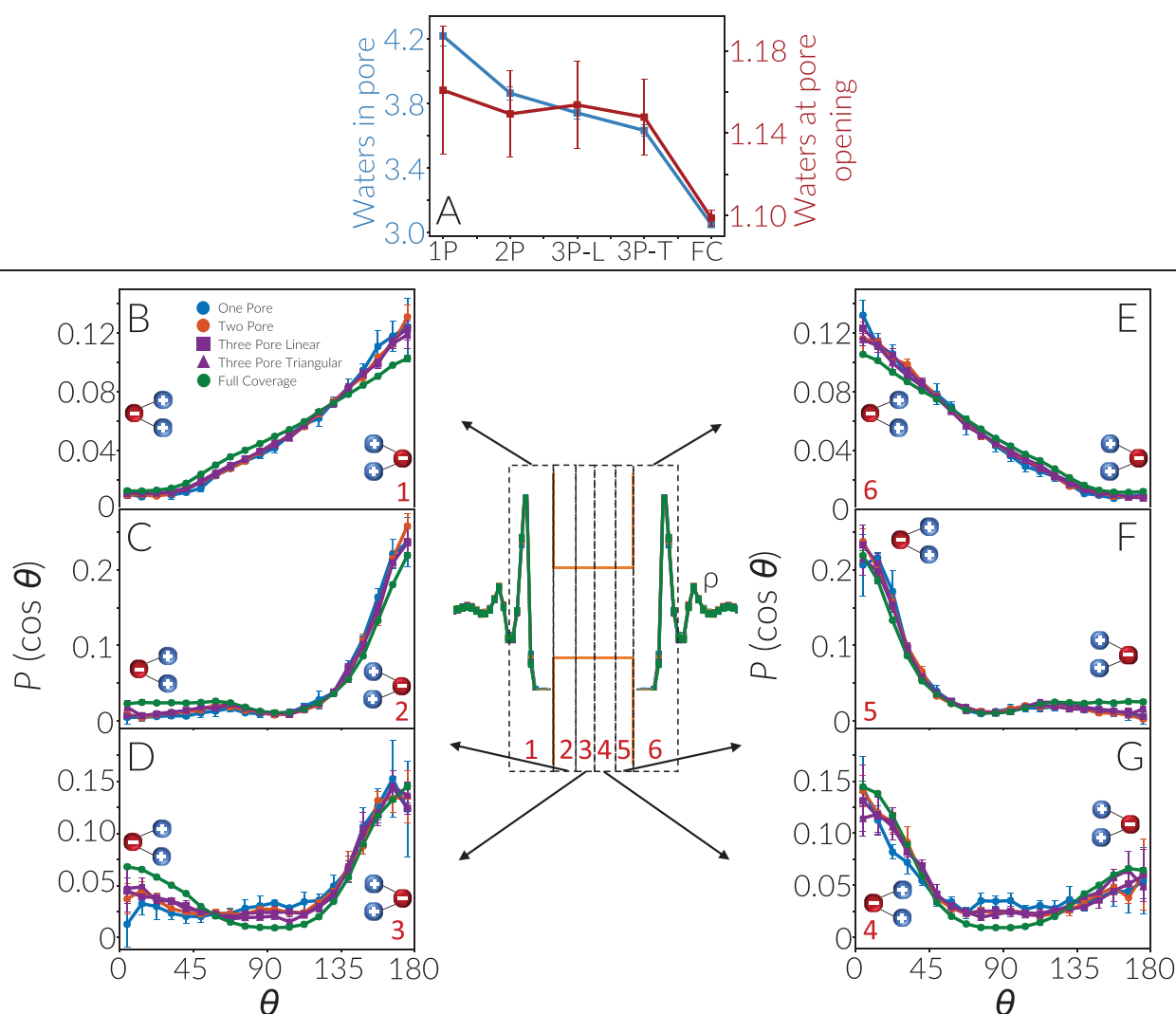
Figure 6. (A) Average number of water molecules in the prepore region and inside the pore. (B−G) Orientational distribution of water molecules in and around the membrane. The curve in the middle corresponds to the water number density as a function of z. For each region highlighted on the density profile, the probability distribution for the angle that water's dipole moments make with the z axis is provided for different pore arrangements. Overall, water molecules tend to adopt orientations in which their oxygens point toward the membrane center, with that tendency weakened in the full coverage system due to interactions with the dipoles of neighboring pores.
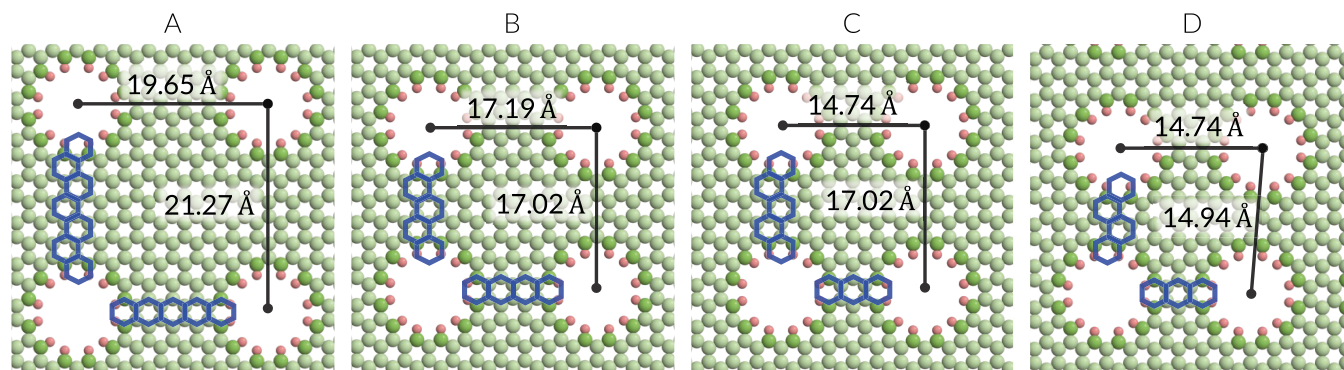
Figure 7. Representative configurations illustrating variations of the full coverage system with different pore densities. In the order of increasing pore density, the systems are labeled as (A) FC4, (B) FC3, (C) FC2X3Y, and (D) FC2-staggered, denoting the number of carbon rings between adjacent pores along the x and y dimensions. In (D), the FC2-staggered configuration slightly diverges from the rectangular arrangement to align with the chemical structure of graphene.

hydration shell and the exit is accompanied by favorable rehydration, the net impact of the dipole−dipole interactions in the one-pore system is to flatten the free energy profile and enhance water permeability. In systems with more pores, however, the alignment of water molecules with the electric field is disrupted, particularly in the full-coverage system, and this attractive force is subsequently weakened. Consequently, fewer water molecules occupy the prepore region and the pore interior (Figure 6A). Furthermore, for water molecules to cross the membrane, they must undergo a dipole moment flip midway along the pore. This flip occurs when water molecules temporarily adopt an orientation within the plane perpendicular to the z axis. The presence of neighboring pore dipoles destabilizes this intermediate orientation. Indeed Figure 6D,G illustrates a noticeable decrease in the probability of observing water molecules at a 90° orientation inside the pores of the full-coverage system, consistent with this mechanism.

All of these observations confirm that increasing pore density has the potential to compromise solvent−solute selectivity by increasing salt flux (via accelerated sodium transport) and decreasing water flux. It is crucial to highlight that the slowdown in water passage occurs on a per-pore basis and the overall permeability of the full coverage system remains higher than that of the single pore system. However, when considering higher pore density as a means of enhancing membrane performance, one should anticipate sublinear scaling of permeability with the number of pores. Additionally, the reduction in the water flux exacerbates the selectivity challenges associated with the increased sodium transport.

Prescreening, Optimization, and Design of Multipore Membranes. The qualitative mechanistic insights obtained from this study provide a fundamental framework for the rational design of innovative membranes. Such efforts can be made more quantitative through utilizing our phenomenological model, which can facilitate high-throughput prescreening of various pore arrangements. Identified promising candidates from this screening process can then be subjected to in-depth exploration, utilizing high-resolution simulations or experimental fabrication for further analysis.

While it might be argued that direct path sampling simulations (using methods such as JFFS) should be used for such screening due to their superior accuracy, it is essential to highlight that such techniques still require conducting relatively lengthy simulations to precisely characterize ion passage rates. Despite their significant reduction in computa-

tional costs compared with conventional MD, these methods present challenges when screening numerous pore configurations for performance evaluation. Conversely, the model outlined in eq 2 involves parameters that are more straightforward to estimate. The change in translocation free energy barrier pertaining to ion−dipole interactions in neighboring pores, denoted as $\Delta\mathcal{E}_{i,n}$, can be readily computed using a simple energy scan. Furthermore, the ion concentration at the pore opening, $\rho_{\mathrm{Cl},i,n}$, is empirically determined from conventional MD simulations within the starting basin and can be effectively converged at a modest computational expense. Notably, in our study, adequate sampling was achieved solely through the basin exploration phase of JFFS.

To illustrate the capability of our model, we conduct several simple optimization exercises. Initially, we investigate the rate of decay of pore−pore correlations with the characteristic separation between nearest-neighbor pores. Four additional pore configurations (depicted in Figure 7) are considered for this analysis, each comprising a rectangular array of pores with varied separations along the x and y directions. The anticipated slowdowns of chloride ions for each system, utilizing the model described in eq 2, are presented in Table 4. Notably, pore−

Table 4. Chloride Slowdown for Different Variants of the Full Coverage System Depicted in Figure 7 Predicted Using eq 2[a]

System	a (nm²)	$\beta\Delta\mathcal{E}_n$	$\rho_{\mathrm{Cl},s}/\rho_{\mathrm{Cl},i,n}$	S_{model}
FC	1.57	1.76	2.37 ± 0.24	13.75 ± 1.39
FC2-staggered	2.19	0.79	1.42 ± 0.15	3.14 ± 0.34
FC2X3Y	2.51	0.64	1.34 ± 0.14	2.56 ± 0.27
FC3	2.93	0.46	1.18 ± 0.12	1.88 ± 0.20
FC4	4.18	0.23	1.11 ± 0.12	1.40 ± 0.15

[a]a refers to the surface area per pore. All uncertainties correspond to 95% confidence intervals.

pore correlations persist across substantial separations, with statistically significant slowdowns present even with three or four carbon rings between neighboring pores. However, a drastic alteration in per-pore passage time is observed as the separation between adjacent pores is reduced from two carbon rings to one (as in the original FC case). To validate the veracity of our model, a full JFFS calculation of chloride translocation time scale is performed in the FC3 system,
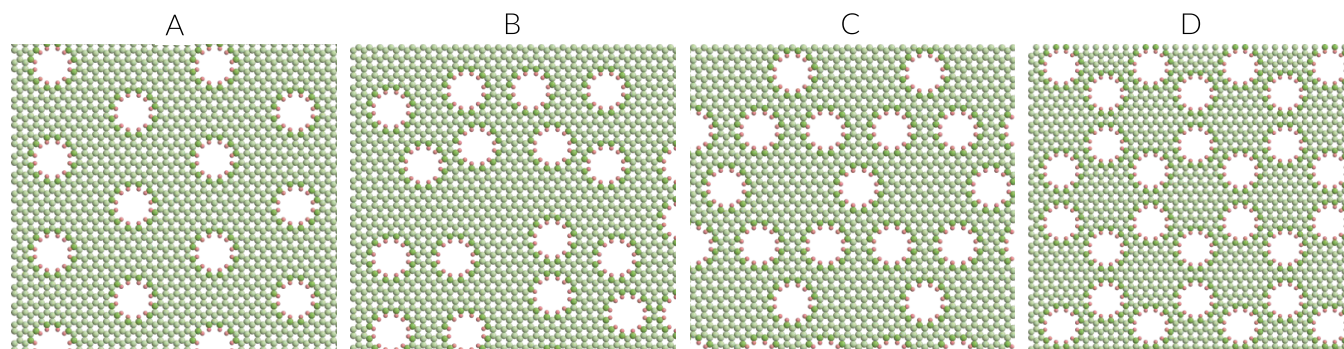
Figure 8. Variations in the pore arrangement at a fixed pore density. Each panel possesses the same pore density as the corresponding panel in Figure 7, but exhibits a distinct pore arrangement: (A) hexagonal lattice, (B) rectangular lattice with individual pores shifted by a single carbon ring along a random direction, (C) kagomé lattice, and (D) honeycomb lattice.

Table 5. Chloride Slowdown for the Pore Arrangements Depicted in Figure 8 Predicted Using eq 2[a]

Arrangement	Parent system	a (nm^2)	$\beta\Delta\mathcal{E}_n$	$\rho_{Cl,s}/\rho_{Cl,i,n}$	S_{model}	S_{rel}
Hexagonal	FC4	3.92	0.25	1.08 ± 0.13	1.38 ± 0.16	0.99 ± 0.07
Randomized	FC3	2.93	0.54	1.37 ± 0.15	2.36 ± 0.26	1.25 ± 0.06
Kagomé	FC2X3Y	2.51	0.75	1.84 ± 0.23	3.88 ± 0.49	1.51 ± 0.13
Honeycomb	FC2-staggered	2.12	1.06	1.98 ± 0.23	5.76 ± 0.68	1.84 ± 0.14

[a]a and S_{rel} refer to surface area per pore and relative slowdown with respect to the parent rectangular arrangement, respectively. All uncertainties correspond to 95% confidence intervals.

yielding a passage time of 3.14 ± 0.19 ns. This corresponds to a slowdown of 2.31 ± 1.04, a value statistically indistinguishable from the prediction obtained by using eq 2.

In a further demonstration of our model's capabilities, we utilize it to optimize pore arrangements at a specific pore density. Considering the adverse effects of pore–pore correlations on solvent–solute selectivity, we propose chloride slowdown as a suitable objective function to minimize for improved membrane performance. We first explore the potential impact of introducing randomness into pore arrangement on pore–pore correlations. To that end, we construct a randomized arrangement (as shown in Figure 8B) by randomly selecting pores from the FC3 system and displacing them from their original positions by one carbon ring along a random direction. This new arrangement yields a marginally increased slowdown of 2.36 compared to the FC3's predicted slowdown of 1.88. This is not surprising considering the nonlinear relationship between pore–pore separation and counterion slowdown. In a randomized arrangement, correlations between pores that are considerably closer than the mean pore–pore separation will dominate the overall slowdown, leading to a decreased performance. It will therefore be more advantageous to construct membranes with regular (e.g., periodic) arrangements of pores.

The next natural inquiry is to discern the ordered configuration that exhibits minimal correlations when the pore density is held constant. Exemplifying this, we investigated the FC4, FC2X3Y, and FC2-staggered systems, endeavoring to devise alternative arrangements based on hexagonal, honeycomb, and kagomé lattices. Given the inherent chemistry of graphene sheets, there exists only a limited number of ways to reorganize pores at a specified density without introducing line defects. Consequently, for each aforementioned system, only *one* alternative arrangement with comparable pore density could be constructed. (No alternative ordered arrangement with comparable pore density

could be obtained in the FC3 system.) Taking the FC4 system as an example, featuring a per-pore area of 4.18 nm^2, we create a hexagonal arrangement with a commensurate per-pore area of 3.92 nm^2 (Figure 8A). The slowdown, as computed from eq 2, is statistically indistinguishable from that of the original rectangular arrangement (1.39 vs 1.40). This can be understood by noting that at a fixed pore density, neighboring pores are anticipated to be marginally more distant in the hexagonal arrangement (specifically, by a factor of $\sqrt{2}/\sqrt[4]{3} \approx 1.075$ in comparison to the perfect square lattice). This is projected to result in diminished pore–pore correlations. However, this effect is counteracted by the presence of more nearest neighbor pores (six vs four) in the hexagonal arrangement. For the FC4 system, these two competing effects cancel out each other. However, either effect might become dominant depending on the target pore density and the scaling of correlations with the pore separation.

Concerning the FC2X3Y and FC2-staggered systems, we successfully construct kagomé (Figure 8C) and honeycomb (Figure 8D) lattices, respectively. In both instances, a notable escalation in pore–pore correlations is evident, as delineated in Table 5. This behavior can be explained by recognizing the inherently larger openness of both lattices compared to the rectangular lattice, leading to significantly closer proximity of the nearest neighbors. Relative to a perfect square lattice, the distance between nearest neighbors in the kagomé and honeycomb lattices decreases by factors of $\sqrt[4]{3}/\sqrt{2} \approx 0.9306$ and $2/\sqrt[4]{27} \approx 0.8774$, respectively. Given the already diminutive pore–pore separations in the FC2X3Y and FC2-staggered systems, this reduction proves sufficient to induce a marked increase in the pore–pore correlation. This underscores the superior efficacy of rectangular (and potentially hexagonal) arrangements compared to their more open-lattice counterparts.

CONCLUSIONS

In this work, we conclusively demonstrate through NEMD simulations and JFFS rate calculations that pore proximity in membranes with dipole-decorated interiors can lead to selective alterations in water and ion transport kinetics (slowdown in water and counterion transport and acceleration in co-ion transport). These changes, resulting from direct dipole-ion and dipole−dipole interactions, significantly deviate from established theories (such as the access resistance model) and ultimately lead to a decrease in solvent−solute selectivity, e.g., in water desalination applications.

Our findings hold crucial implications for the development of membrane technologies aimed at efficient separation of ionic solutes from polar solvents, specifically in water desalination. Increasing the pore density within nanoporous membranes may initially appear as a viable approach to enhance solvent permeation without affecting ion−solvent selectivity. However, the direct interactions between ions and solvent molecules with partial charges in neighboring pores can compromise the membrane selectivity. Therefore, the strategy of optimizing the performance of isolated pores and subsequently integrating a large number of them into a porous membrane may not be viable. Instead, it is imperative to quantify pore−pore correlations carefully and approach the design of ultraselective membranes as an optimization problem, considering all such correlations and the tradeoffs between sublinear permeability and decline in selectivity.

Our observations also highlight the importance of properly designing and conducting computational investigations of selectivity, especially when comparing with experimental results. It is indeed crucial to closely match the pore density and arrangement between simulations and experiments in order to avoid spurious discrepancies that may arise from differing pore separations in otherwise identical systems.

While our investigation primarily focuses on graphene-based nanoporous membranes, we assert that our findings hold broader relevance and are applicable to any nanopore that is narrow enough to engender activated ion transport. This generalizability is underpinned by the fundamental observation that any covalent bond linking two distinct atoms inherently possesses a dipole moment and the fact that most nanopores feature interiors decorated with such covalent bonds, exhibiting varying degrees of polarity. Indeed, it is worth noting that the extent of pore−pore correlations depends on various factors, including the strength and number of dipoles within each pore. In our study, we specifically consider C−H bonds, which possess a modest dipole moment of 0.6 D and are thus categorized as moderately polar. Nevertheless, it is still notable that significant pore−pore correlations endure, even at substantial separations. For nanopores characterized by more polar interior environments, we anticipate even more pronounced correlations, extending over greater length scales and making permeability and selectivity even more susceptible to pore density. Additionally, the presence of anisotropic patterning and heterogeneous membranes with varying pore sizes and chemistries could offer a promising strategy to tune the magnitude and direction of the pore−pore interactions.

Considering the short-range nature of ion−dipole interactions, these correlations will become relevant only when the characteristic separation between neighboring pores is on the order of nanometers. Such nanometer-scale porosity is attainable across a range of membranes, spanning from those composed of 2D materials such as graphene to zeolites, metal−organic frameworks, biological channel proteins, and biomimetic nanopores. The elucidation of these correlations by our study therefore holds immense relevance and applicability to the rational design of high-porosity membranes across various material types and diverse applications.

The observed pore−pore correlations, similar to other electrostatic interactions, can be screened within a dielectric medium, with the effectiveness of screening depending on the membrane's dielectric constant. The low dielectric constants of the model membranes considered in this work result in significant correlations. Considering flexible membranes and polarizable force fields or modifying interior chemistry and pore arrangements may, however, attenuate these correlations, necessitating their consideration in efforts to control and engineer pore−pore interactions.

Since the pore−pore correlations discovered in this work arise due to ion−dipole interactions, their occurrence is unlikely to depend on the particular driving forces present in a system. Therefore, while we confirm their presence in a system under pressure and chemical potential gradients, these correlations are anticipated to persist across various modes of transport, including scenarios involving electric fields. However, the magnitude of such correlations may vary owing to the influence of an electric field on the prepore concentrations of different ions and the polarity of bonds within neighboring pore interiors. It is necessary to note that the latter effect can be captured only through simulations using polarizable force fields.

One of the more interesting applications of nanoporous membranes is their use in ion−ion separation. It is therefore imperative to discuss how the presence of multiple ion types within the feed will impact the pore−pore correlations uncovered in this work. When an ion has already entered the pore, the amount of slowdown (or acceleration) that it experiences will depend on only its charge. Consequently, notable differential correlations will chiefly emerge among ions with different valences such as mixtures comprising monovalent and divalent ions. When it comes to the partitioning of ions into the prepore region, however, considerable distinctions might arise even among ions with identical valences. This is because the introduction of a second ion, even with an identical charge, can induce large changes in the prepore concentration of a specific ion. Hence, altering the pore density could potentially serve as a viable approach to modulate ion−ion selectivity. However, the formulation of precise design principles for this process cannot rely solely on electrostatic considerations. Further comprehensive studies are crucial to establishing and elucidating these design guidelines.

Our findings extend beyond the design of nanoporous membranes for separation applications and offer valuable insights into the behavior of nanoporous membranes in natural systems. Notably, this includes biological cells that utilize ion channels on their membranes to regulate ion transport and establish the desired reversal potentials across cellular and organellar membranes. Reversal potentials arise due to differential preference of a membrane toward anions and cations and can be predicted using the Goldman−Hodgkin−Katz equation.[44] The pores considered in this work also exert such a preference and will therefore possess a reversal potential. The pore−pore correlations observed here will dampen the reversal potential by closing the gap between counterion and co-ion fluxes. Such correlations are expected to

emerge in biological channels as well, since the interiors of biological channels are almost always decorated with polar bonds. The potential physiological impacts of such correlations can be profound. Indeed, cells employ the modulation of channel density, achieved through changes to gene expression, as a means of controlling the reversal potential to achieve specific physiological outcomes. Recently, there has been an increased focus on the implications of correlations and cooperativity among biological channels on physiological function.[45] For instance, spatial clustering of Kv2.1 potassium channels in neurons' somatodendritic domains has been shown to attenuate their excitability.[46] While the precise mechanisms of such correlations remain a subject of ongoing exploration, the type of pore−pore correlation observed here may offer insights into the explanation of these intricate nonlinear relationships between channel density and physiological responses. Therefore, fundamental studies of this nature hold the promise of unraveling complex nonlinear outcomes in biological systems.

METHODS

System Setup. The construction and simulation techniques employed in this work closely follow the methods described in refs 5 and 6. The membranes under consideration consist of hydrogen-passivated nanoporous graphene sheets. Pristine armchair graphene sheets are initially generated using the `Nanotube Builder` feature of VMD.[47] Pores are created by removing carbon atoms within a radius of 4.3 Å from the center of a specific hexagonal ring. Hydrogen atoms are then added to satisfy the dangling bonds at the pore edges, positioned 1.09 Å away from the remaining carbon atoms along the connecting vector with their missing neighbors (see Figure 1A). The complete membrane is assembled by duplicating the first sheet twice, with a separation of 3.35 Å and a parallel shift of 1.418 Å, following the graphite stacking structure. In multipore membranes, proximal pores are separated by an integer number of carbon rings. The study encompasses five distinct pore arrangements: *one-pore (1P)*, *two-pore (2P)*, *three-pore linear (3PL)*, *three-pore triangular (3PT)*, and *full coverage (FC)* (see Figure 1C−G). (In addition to the FC system in which adjacent pores are separated by a single carbon ring, we consider other full coverage arrangements as discussed in the text and depicted in Figures 7 and 8.) Following membrane setup, nonporous graphene sheets are introduced on both sides of the membrane to enclose the system and serve as pistons. Water and salt ions are then incorporated into the system using PACKMOL.[48] Figure 1B illustrates the setup, wherein the larger compartment represents the feed reservoir, containing water molecules and sodium and chloride ions while the filtrate consists solely of water molecules. All renderings of individual configurations have been generated using `injavis`.[49] To ensure sufficient sampling of the configuration space, different seeds are employed in PACKMOL to generate 100 and 200 independent configurations for single-pore and multipore membranes, respectively. Each configuration therefore possesses an uncorrelated arrangement of water molecules and salt ions. Further information including the number of molecules and ions and the dimensions of the membranes is given in Table S1 in the Supporting Information.

Molecular Dynamics Simulations. We represent all atoms as charged Lennard−Jones (LJ) particles with partial charges and LJ parameters for water molecules and sodium and chloride ions chosen from TIP3P[50] and Joung−Cheatham (JC)[51] force fields, respectively. For carbon and hydrogen atoms in the membrane and pistons, we use the parameters given by Beu[52] and Müller-Plathe.[53] These force fields assign partial charges of $-0.115e$ and $+0.115e$ to the carbon and hydrogen atoms at the pore interiors, respectively. We confirmed the accuracy of these values using direct density functional theory (DFT) calculations in a prior study.[6] This yields a dipole moment of 0.6 D for each C−H bond, which is in line with experimental observations

for C−H bonds connected to aromatic carbons.[54] Molecular dynamics (MD) trajectories are conducted using LAMMPS,[55] with the velocity Verlet algorithm[56] used for integrating equations of motion. The membrane atoms remain fixed throughout the simulations to ensure computational efficiency, while water molecules' rigidity is maintained using the SHAKE algorithm.[57] Long-range electrostatic interactions are treated using the slab particle−particle particle mesh (PPPM) method[58] with periodic boundary conditions applied in the x and y directions only. A Nosé−Hoover thermostat[59,60] with a damping time constant of 0.1 ps is employed to maintain the temperature of water molecules and salt ions at 300 K. During equilibration, the system is simulated in the canonical ensemble with a time step of 0.5 fs for 0.1 ns, while the pistons are held fixed. Following this initial relaxation, the time step is increased to 1 fs. The pistons are then allowed to move as rigid bodies in the z direction, and a pressure gradient of 194 atm is applied using the LAMMPS fix `aveforce` command. With the mobile pistons, the trajectories are extended for an additional 2 ns to generate equilibrated structures.

Path Sampling Simulations. Since ion transport through subnanometer pores is a rare event and can occur over time scales inaccessible to conventional NEMD simulations, we utilize our recently developed JFFS algorithm[30] to probe such extended time scales. Technical details, including the description of the order parameter, can be found in our earlier publications.[5,6,61] Our focus lies on transitions of the type $F_{p,q} \rightarrow F_{p\pm1,q\pm1}$, where $F_{p,q}$ denotes the state with p sodium ions and q chloride ions present in the filtrate. Finite size effects strongly influence nonequilibrium ion transport, as extensively discussed in our recent work.[6] Therefore, we adopt the ideal conductor/dielectric model (ICDM) proposed and validated in our recent publication[62] to determine free energy barriers and passage times in the thermodynamic limit (Tables S2 and S3 in the Supporting Information). Since multipore membranes may contain significant amounts of water, estimating the dielectric constant of the hydrated membrane becomes crucial for the finite size correction. We compute the dielectric constant using the approach described by Neumann,[63] which involves calculating fluctuations of the dipole moment ($\mathbf{M}$) of all water molecules within the membrane region. The average dielectric constant is obtained using the formula

$$\varepsilon = 1 + \frac{\langle|\mathbf{M}|^2\rangle - |\langle\mathbf{M}\rangle|^2}{3\varepsilon_0 k_b T \langle V \rangle} \tag{4}$$

Here, ε_0 represents the vacuum permittivity, k_b is the Boltzmann constant, and $\langle V \rangle$ denotes the volume of the membrane region. To avoid unphysical spikes in the dipole moment when a water molecule partially occupies the membrane, when the oxygen atom falls within the membrane region, the entire molecule is included in calculating $\mathbf{M}$, and it is excluded otherwise.

ASSOCIATED CONTENT

Data Availability Statement

An earlier preprint of this manuscript is available at ChemRXiv: Shoemaker, B. S.; Khalifa, O.; Haji-Akbari, A. Correlations in charged multipore systems: Implications for enhancing selectivity and permeability in nanoporous membranes. 2023, 10.26434/chemrxiv-2023-n1qx2. ChemRxiv. Cambridge: Cambridge Open Engage. https://dx.doi.org/10.26434/chemrxiv-2023-n1qx2 (November 29, 2023).

Ⓢ Supporting Information

The Supporting Information is available free of charge at https://pubs.acs.org/doi/10.1021/acsnano.3c07489.

> Further details about the uncertainty analysis in the application of the access resistance model, a figure on the convergence of dielectric constant calculations, and several tables on system specifics and the application of the ideal conductor/dielectric model (PDF)

AUTHOR INFORMATION

Corresponding Author

Amir Haji-Akbari − *Department of Chemical and Environmental Engineering, Yale University, New Haven, Connecticut 06511, United States;* ⊙ orcid.org/0000-0002-2228-6957; Email: amir.hajiakbaribalou@yale.edu

Authors

Brian A. Shoemaker − *Department of Chemical and Environmental Engineering, Yale University, New Haven, Connecticut 06511, United States*

Omar Khalifa − *Department of Chemical and Environmental Engineering, Yale University, New Haven, Connecticut 06511, United States*

Complete contact information is available at:
https://pubs.acs.org/10.1021/acsnano.3c07489

Notes

The authors declare no competing financial interest.

REFERENCES

(1) Wang, L.; He, J.; Heiranian, M.; Fan, H.; Song, L.; Li, Y.; Elimelech, M. Water transport in reverse osmosis membranes is governed by pore flow, not a solution-diffusion mechanism. *Sci. Adv.* **2023**, *9*, eadf8488.

(2) Aluru, N. R.; Aydin, F.; Bazant, M. Z.; Blankschtein, D.; Brozena, A. H.; de Souza, J. P.; Elimelech, M.; Faucher, S.; Fourkas, J. T.; Koman, V. B.; et al. others Fluids and electrolytes under confinement in single-digit nanopores. *Chem. Rev.* **2023**, *123*, 2737−2831.

(3) Han, Y.; Xu, Z.; Gao, C. Ultrathin Graphene Nanofiltration Membrane for Water Purification. *Adv. Funct. Mater.* **2013**, *23*, 3693−3700.

(4) Cohen-Tanugi, D.; Grossman, J. C. Water Desalination across Nanoporous Graphene. *Nano Lett.* **2012**, *12*, 3602−3608.

(5) Malmir, H.; Epsztein, R.; Elimelech, M.; Haji-Akbari, A. Induced charge anisotropy: A hidden variable affecting ion transport through membranes. *Matter* **2020**, *2*, 735−750.

(6) Shoemaker, B. A.; Domingues, T. S.; Haji-Akbari, A. Ideal Conductor Model: An Analytical Finite-Size Correction for Nonequilibrium Molecular Dynamics Simulations of Ion Transport through Nanoporous Membranes. *J. Chem. Theory Comput.* **2022**, *18*, 7142−7154.

(7) Yang, S.; Ryu, I.; Kim, H.; Kim, J.; Jang, S.; Russell, T. Nanoporous Membranes with Ultrahigh Selectivity and Flux for the Filtration of Viruses. *Adv. Mater.* **2006**, *18*, 709−712.

(8) Lu, X.; Feng, X.; Yang, Y.; Jiang, J.; Cheng, W.; Liu, C.; Gopinadhan, M.; Osuji, C. O.; Ma, J.; Elimelech, M. Tuning the permselectivity of polymeric desalination membranes via control of polymer crystallite size. *Nat. Commun.* **2019**, *10*, 2347.

(9) Ravi, J.; Othman, M. H. D.; Matsuura, T.; Ro'il Bilad, M.; Elbadawy, T.; Aziz, F.; Ismail, A.; Rahman, M. A.; Jaafar, J. Polymeric membranes for desalination using membrane distillation: A review. *Desalination* **2020**, *490*, 114530.

(10) Chu, K.-L.; Shannon, M. A.; Masel, R. I. An Improved Miniature Direct Formic Acid Fuel Cell Based on Nanoporous Silicon for Portable Power Generation. *J. Electrochem. Soc.* **2006**, *153*, A1562.

(11) Tong, H. D.; Jansen, H. V.; Gadgil, V. J.; Bostan, C. G.; Berenschot, E.; van Rijn, C. J. M.; Elwenspoek, M. Silicon Nitride Nanosieve Membrane. *Nano Lett.* **2004**, *4*, 283−287.

(12) Osmanbeyoglu, H. U.; Hur, T. B.; Kim, H. K. Thin alumina nanoporous membranes for similar size biomolecule separation. *J. Membr. Sci.* **2009**, *343*, 1−6.

(13) Vlassiouk, I.; Krasnoslobodtsev, A.; Smirnov, S.; Germann, M. Direct" Detection and Separation of DNA Using Nanoporous Alumina Filters. *Langmuir* **2004**, *20*, 9913−9915.

(14) Ma, S.; Zhou, H.-C. Gas storage in porous metal−organic frameworks for clean energy applications. *Chem. Commun.* **2010**, *46*, 44−53.

(15) Yoon, M.; Srirambalaji, R.; Kim, K. Homochiral Metal−Organic Frameworks for Asymmetric Heterogeneous Catalysis. *Chem. Rev.* **2012**, *112*, 1196−1231.

(16) Orellana-Tavra, C.; Baxter, E. F.; Tian, T.; Bennett, T. D.; Slater, N. K. H.; Cheetham, A. K.; Fairen-Jimenez, D. Amorphous metal−organic frameworks for drug delivery. *Chem. Commun.* **2015**, *51*, 13878−13881.

(17) Horcajada, P.; Serre, C.; Maurin, G.; Ramsahye, N. A.; Balas, F.; Vallet-Regí, M.; Sebban, M.; Taulelle, F.; Férey, G. Flexible Porous Metal-Organic Frameworks for a Controlled Drug Delivery. *J. Am. Chem. Soc.* **2008**, *130*, 6774−6780.

(18) Li, H.; Eddaoudi, M.; Groy, T. L.; Yaghi, O. Establishing microporosity in open metal- organic frameworks: gas sorption isotherms for Zn (BDC)(BDC= 1, 4-benzenedicarboxylate). *J. Am. Chem. Soc.* **1998**, *120*, 8571−8572.

(19) Sumida, K.; Rogow, D. L.; Mason, J. A.; McDonald, T. M.; Bloch, E. D.; Herm, Z. R.; Bae, T.-H.; Long, J. R. Carbon Dioxide Capture in Metal−Organic Frameworks. *Chem. Rev.* **2012**, *112*, 724−781.

(20) Canepa, P.; Arter, C. A.; Conwill, E. M.; Johnson, D. H.; Shoemaker, B. A.; Soliman, K. Z.; Thonhauser, T. High-throughput screening of small-molecule adsorption in MOF. *J. Mater. Chem. A* **2013**, *1*, 13597−13604.

(21) Wang, L.; Wang, Z.; Patel, S. K.; Lin, S.; Elimelech, M. Nanopore-based power generation from salinity gradient: why it is not viable. *ACS Nano* **2021**, *15*, 4093−4107.

(22) Qasim, M.; Badrelzaman, M.; Darwish, N. N.; Darwish, N. A.; Hilal, N. Reverse osmosis desalination: A state-of-the-art review. *Desalination* **2019**, *459*, 59−104.

(23) Fritzmann, C.; Löwenberg, J.; Wintgens, T.; Melin, T. State-of-the-art of reverse osmosis desalination. *Desalination* **2007**, *216*, 1−76.

(24) Peñate, B.; García-Rodríguez, L. Current trends and future prospects in the design of seawater reverse osmosis desalination technology. *Desalination* **2012**, *284*, 1−8.

(25) Biesheuvel, P. M.; Zhang, L.; Gasquet, P.; Blankert, B.; Elimelech, M.; van der Meer, W. G. J. Ion Selectivity in Brackish Water Desalination by Reverse Osmosis: Theory, Measurements, and Implications. *Envir. Sci. Technol. Lett.* **2020**, *7*, 42−47.

(26) Park, H. B.; Kamcev, J.; Robeson, L. M.; Elimelech, M.; Freeman, B. D. Maximizing the right stuff: The trade-off between membrane permeability and selectivity. *Science* **2017**, *356*, eaab0530.

(27) Hille, B. Pharmacological Modifications of the Sodium Channels of Frog Nerve. *J. Gen. Physiol.* **1968**, *51*, 199−219.

(28) Hall, J. E. Access resistance of a small circular pore. *J. Gen. Physiol.* **1975**, *66*, 531−532.

(29) Nguyen, T. D.; Carrillo, J.-M. Y.; Dobrynin, A. V.; Brown, W. M. A case study of truncated electrostatics for simulation of polyelectrolyte brushes on GPU accelerators. *J. Chem. Theory Comput.* **2013**, *9*, 73−83.

(30) Haji-Akbari, A. Forward-flux sampling with jumpy order parameters. *J. Chem. Phys.* **2018**, *149*, No. 072303.

(31) Lucas, R. A.; Siwy, Z. S. Tunable Nanopore Arrays as the Basis for Ionic Circuits. *ACS Appl. Mater. Interfaces* **2020**, *12*, 56622−56631.

(32) Gadaleta, A.; Sempere, C.; Gravelle, S.; Siria, A.; Fulcrand, R.; Ybert, C.; Bocquet, L. Sub-additive ionic transport across arrays of solid-state nanopores. *Phys. Fluids* **2014**, *26*, No. 012005.

(33) Sahu, S.; Zwolak, M. Golden aspect ratio for ion transport simulation in nanopores. *Phys. Rev. E* **2018**, *98*, No. 012404.

(34) Peskoff, A.; Bers, D. Electrodiffusion of ions approaching the mouth of a conducting membrane channel. *Biophys. J.* **1988**, *53*, 863−875.

(35) Aguilella-Arzo, M.; Aguilella, V. M.; Eisenberg, R. Computing numerically the access resistance of a pore. *Euro. Biophys. J.* **2005**, *34*, 314−322.

(36) Luchinsky, D.; Tindjong, R.; Kaufman, I.; McClintock, P.; Eisenberg, R. Self-consistent analytic solution for the current and the access resistance in open ion channels. *Phys. Rev. E* **2009**, *80*, No. 021925.

(37) Tsutsui, M.; Yokota, K.; Nakada, T.; Arima, A.; Tonomura, W.; Taniguchi, M.; Washio, T.; Kawai, T. Electric field interference and bimodal particle translocation in nano-integrated multipores. *Nanoscale* **2019**, *11*, 7547−7553.

(38) Xiao, F.; Ji, D.; Li, H.; Tang, J.; Feng, Y.; Ding, L.; Cao, L.; Li, N.; Jiang, L.; Guo, W. A general strategy to simulate osmotic energy conversion in multi-pore nanofluidic systems. *Mater. Chem. Front.* **2018**, *2*, 935−941.

(39) Kosińska, I. D.; Goychuk, I.; Kostur, M.; Schmid, G.; Hänggi, P. Rectification in synthetic conical nanopores: A one-dimensional Poisson-Nernst-Planck model. *Phys. Rev. E* **2008**, *77*, No. 031131.

(40) Jeong, H.-I.; Kim, H. J.; Kim, D.-K. Numerical analysis of transport phenomena in reverse electrodialysis for system design and optimization. *Energy* **2014**, *68*, 229−237.

(41) Bazant, M. Z.; Thornton, K.; Ajdari, A. Diffuse-charge dynamics in electrochemical systems. *Phys. Rev. E* **2004**, *70*, No. 021506.

(42) Kosińska, I. D.; Goychuk, I.; Kostur, M.; Schmid, G.; Hänggi, P. Rectification in synthetic conical nanopores: A one-dimensional Poisson-Nernst-Planck model. *Phys. Rev. E* **2008**, *77*, No. 031131.

(43) Thapar, V.; Escobedo, F. A. Simultaneous estimation of free energies and rates using forward flux sampling and mean first passage times. *J. Chem. Phys.* **2015**, *143*, 244113.

(44) Hodgkin, A. L.; Huxley, A. F.; Katz, B. Measurement of current-voltage relations in the membrane of the giant axon of Loligo. *J. Physiol.* **1952**, *116*, 424.

(45) Dixon, R. E.; Navedo, M. F.; Binder, M. D.; Santana, L. F. Mechanisms and physiological implications of cooperative gating of clustered ion channels. *Physiol. Rev.* **2022**, *102*, 1159−1210.

(46) Misonou, H.; Mohapatra, D. P.; Park, E. W.; Leung, V.; Zhen, D.; Misonou, K.; Anderson, A. E.; Trimmer, J. S. Regulation of ion channel localization and phosphorylation by neuronal activity. *Nat. Neurosci.* **2004**, *7*, 711−718.

(47) Humphrey, W.; Dalke, A.; Schulten, K. VMD: visual molecular dynamics. *J. Mol. Graphics* **1996**, *14*, 33−38.

(48) Martínez, L.; Andrade, R.; Birgin, E. G.; Martínez, J. M. PACKMOL: A package for building initial configurations for molecular dynamics simulations. *J. Comput. Chem.* **2009**, *30*, 2157−2164.

(49) Engel, M. INJAVIS — INteractive JAva VISualization. *Zenodo* **2021**, 4639570.

(50) Price, D. J.; Brooks, C. L. A modified TIP3P water potential for simulation with Ewald summation. *J. Chem. Phys.* **2004**, *121*, 10096−10103.

(51) Joung, I. S.; Cheatham, T. E. I. Determination of Alkali and Halide Monovalent Ion Parameters for Use in Explicitly Solvated Biomolecular Simulations. *J. Phys. Chem. B* **2008**, *112*, 9020−9041.

(52) Beu, T. A. Molecular dynamics simulations of ion transport through carbon nanotubes. I. Influence of geometry, ion specificity, and many-body interactions. *J. Chem. Phys.* **2010**, *132*, 164513.

(53) Müller-Plathe, F. Local structure and dynamics in solvent-swollen polymers. *Macromolecules* **1996**, *29*, 4782−4791.

(54) Cole, A.; Michell, A. The dipole moment of the C-H bond in benzene derivatives from infrared intensities. *Spectrochim. Acta* **1964**, *20*, 739−746.

(55) Plimpton, S. Short-Range Molecular Dynamics. *J. Comput. Phys.* **1995**, *117*, 1−42.

(56) Swope, W. C.; Andersen, H. C.; Berens, P. H.; Wilson, K. R. A computer simulation method for the calculation of equilibrium constants for the formation of physical clusters of molecules: Application to small water clusters. *J. Chem. Phys.* **1982**, *76*, 637−649.

(57) Andersen, H. C. Rattle: A "velocity" version of the shake algorithm for molecular dynamics calculations. *J. Comput. Phys.* **1983**, *52*, 24−34.

(58) Bostick, D.; Berkowitz, M. L. The implementation of slab geometry for membrane-channel molecular dynamics simulations. *Biophys. J.* **2003**, *85*, 97−107.

(59) Nosé, S. A molecular dynamics method for simulations in the canonical ensemble. *Mol. Phys.* **1984**, *52*, 255−268.

(60) Hoover, W. G. Canonical dynamics: Equilibrium phase-space distributions. *Phys. Rev. A* **1985**, *31*, 1695−1697.

(61) Hussain, S.; Haji-Akbari, A. Studying rare events using forward-flux sampling: Recent breakthroughs and future outlook. *J. Chem. Phys.* **2020**, *152*, No. 060901.

(62) Shoemaker, B. A.; Haji-Akbari, A. Ideal conductor/dielectric model (ICDM): A generalized technique to correct for finite-size effects in molecular simulations of hindered ion transport. *J. Chem. Phys.* **2024**, https://doi.org/10.1063/5.0180029.

(63) Neumann, M. Dipole moment fluctuation formulas in computer simulations of polar systems. *Mol. Phys.* **1983**, *50*, 841−858.